ACS OMEGA

Article

Cite This: ACS Omega 2017, 2, 9074−9079

Effect of Cs-Incorporated NiO$_x$ on the Performance of Perovskite Solar Cells

Hui-Seon Kim,*[†] Ji-Youn Seo,[‡] Haibing Xie,[§] Monica Lira-Cantu,[§] Shaik M. Zakeeruddin,[‡] Michael Grätzel,[‡] and Anders Hagfeldt*[†]

[†]Laboratory of Photomolecular Science, Institute of Chemical Sciences and Engineering, School of Basic Sciences, and [‡]Laboratory for Photonics and Interfaces, Institute of Chemical Sciences and Engineering, School of Basic Sciences, Ecole Polytechnique Fédérale de Lausanne, CH-1015 Lausanne, Switzerland

[§]Catalan Institute of Nanoscience and Nanotechnology (ICN2), CSIC and the Barcelona Institute of Science and Technology (BIST). Building ICN2, Campus UAB, Bellaterra, E-08193 Barcelona, Spain

Supporting Information

ABSTRACT: The effect of Cs-incorporated NiO$_x$ on perovskite solar cells with an inverted structure was investigated, where NiO$_x$ and PCBM were used as selective contacts for holes and electrons, respectively. It was found that the generation of an Ni phase in an NiO$_x$ layer was significantly suppressed by employing cesium. Furthermore, Cs-incorporated NiO$_x$ enabled holes to be efficiently separated at the interface, showing the improved photoluminescent quenching and thus generating higher short-circuit current. The effect of Cs incorporation was also prominent in the inhibition of recombination. The recombination resistance of Cs-incorporated NiO$_x$ was noticeably increased by more than three-fold near the maximum power point, leading to a higher fill factor of 0.78 and consequently a higher power conversion efficiency of 17.2% for the device employing Cs-incorporated NiO$_x$.

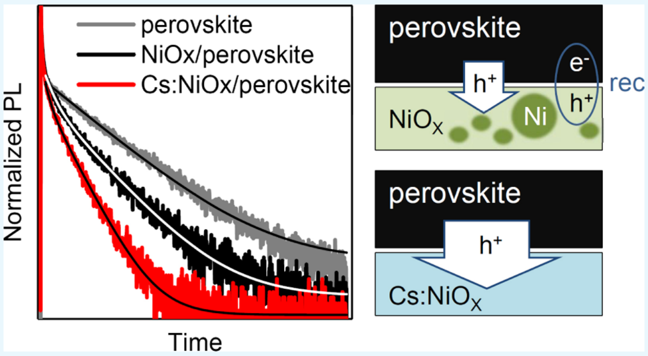

INTRODUCTION

Since 2012, the perovskite solar cells unexpectedly have been attracting interest owing to their remarkable potential for high efficiency and stability,[1,2] and intensive studies on perovskite solar cells have been extensively carried out, leading to outstanding achievements in terms of efficiency, stability, and understanding of underlying mechanisms. Various methods have been successfully developed to enhance the quality of the perovskite layer by controlling the film growth.[3−8] Among them, the adduct[8] and the antisolvent[4] methods became the two most popular methods for the current technology of high-efficiency perovskite solar cells. Furthermore, multiple cations, such as methylammonium (MA$^+$), formamidinium (FA$^+$), cesium (Cs$^+$), and rubidium (Rb$^+$), were efficiently incorporated into the perovskite to stabilize its phase as well as to achieve the high efficiency of 21.6%.[9] The most common perovskite configuration which has been intensively studied is the normal structure based on TiO$_2$ as an electron transport layer and 2,2′,7,7′-tetrakis (*N*,*N*-di-*p*-methoxyphenylamine)-9,9′-spirobifluorene (spiro-MeOTAD) as a hole transport layer. Even though the perovskite device with a TiO$_2$/perovskite/spiro-MeOTAD structure is the one used in the efficiency chart,[10] it still has certain problems to be solved. It was found that those selective contacts, TiO$_2$ and spiro-MeOTAD, coupled with halide perovskites, induced time-dependent behaviors,[11−16] which are sufficiently observable in the range of solar cell operation, such as *I*−*V* hysteresis[11−14] and/or interfacial dynamics related to the ion migration from the perovskite bulk layer.[13−16] These complicating mechanisms at the interface are not fully understood and also imply the negative effect on long-term stability.[16,17] Also, spiro-MeOTAD itself is easily crystallized at high temperatures,[18,19] underlying limitations on future commercial development. Unlike the normal structure, the inverted structure employing NiO$_x$ and [6,6]-phenyl-C$_{60}$-butyric acid methyl ester (PCBM) as hole and electron selective contacts demonstrated superb air and thermal stability[18] with hysteresis-free characteristics based on its fast response time.[14] Besides, many efforts have been made on achieving high efficiency close to that of the normal structure.[20−22] Since the initial works on the inverted structure with NiO$_x$ and PCBM in 2014 to replace unstable organic hole transport layers and obtain better energy level alignment,[23−25] Mg and Li co-doping was tried to increase the conductivity of NiO$_x$ as well as tune the band alignment with perovskites, which resulted in a power conversion efficiency (PCE) of 16.2%.[20] Cu-doped NiO$_x$ was also reported and demonstrated 17.8% of perovskite solar cells because of its high crystallinity and improved conductivity.[21] Nevertheless, a few papers were

Received: September 7, 2017
Accepted: December 1, 2017
Published: December 18, 2017

DOI: 10.1021/acsomega.7b01179
ACS Omega 2017, 2, 9074−9079

published compared to the normal structure where every single selective contact was carefully engineered to enhance the performance. In this study, cesium is employed in the NiO_x layer to improve the performance of the inverted perovskite solar cells. The effect of cesium is investigated in respect of the inhibition of Ni phase formation in the NiO_x bulk layer as well as the efficient charge-transfer behavior at the NiO_x/perovskite interface. In the end, both aspects are closely related to the photovoltaic performance.

■ RESULTS AND DISCUSSION

Figure 1a shows X-ray diffraction (XRD) patterns of NiO_x and Cs-incorporated NiO_x powders. To collect the powders for XRD measurements, the NiO_x precursor solutions were prepared and heated in the same manner as the NiO_x layer for devices. XRD peaks shown at 37.18°, 43.25°, and 62.86° (blue vertical lines in Figure 1a) correspond respectively to (111), (200), and (220) planes of the NiO phase according to JCPDS (22-1189). It is noted that an Ni metal phase is observed from the NiO_x sample at 44.5° and 51.8° (red vertical lines in Figure 1a) corresponding to (111) and (200) planes for Ni.[26] A ratio quantification of Ni to NiO was obtained by the Rietveld refinement, showing a ratio of 0.16:0.84. Interestingly, the Ni impurity is significantly suppressed by employing 1 mol % cesium in the precursor solution (Cs/NiO_x). It was confirmed by the energy-dispersive X-ray spectroscopy (EDXS), showing that 0.7 at. % Cs was included in NiO_x. The ionic radii of $Ni^{2+}$and Cs^+ were found to be 0.69 and 1.67 Å, respectively.[27,28] When considering the large size difference between them, it is difficult to substitute Cs^+ for Ni^{2+} as in the general Li^+ doping. Nevertheless, cesium nickel oxide, $Cs_{0.1}NiO_2$, has the same crystal system and space group as NiO (Table S1), which suggests that a small amount of Cs might occupy Ni vacancies and be incorporated to the NiO_x lattice. Because the error range for the XRD measurement used in this study is within $2\theta \leq \pm 0.0065°$, the peak shift from 43.31° to 43.28° indicates the slight increase of the lattice parameter due to the larger size of Cs^+ compared to the Ni^{2+}. X-ray photoelectron spectroscopy (XPS) spectra of nickel oxide are shown in Figure 1b, where peaks near 872 and 854 eV are attributed to Ni $2p_{2/1}$ and Ni $2p_{3/2}$, respectively. Ni $2p_{3/2}$ XPS spectra incorporate Ni^{2+} at 854.5 eV and Ni^{3+} at 855.8 eV for both NiO_x and Cs-incorporated NiO_x (Cs/NiO_x),[29] which implies that both NiO and Ni_2O_3 phases are mixed in nickel oxide irrespective of Cs incorporation. It is noted that Ni^0 at 852.9 eV is not clearly seen in Ni $2p_{3/2}$ XPS spectra for NiO_x employing the Ni phase (Figure 1a), suggesting that the Ni phase is formed from bulk NiO_x and leaves the oxidized form (NiO_x) on the surface. In Figure S1, the Ni^0 peak is observed from the NiO_x sample after milling, indicating the presence of Ni^0 inside bulk. In Figure 1c, XPS peaks corresponding to Cs $3d_{3/2}$ (738.4 eV) and Cs $3d_{5/2}$ (724.6 eV) are clearly observed from Cs/NiO_x, while NiO_x shows the absence of Cs 3d spectra.[30] The XPS result of Cs/NiO_x indicates that 0.8 at. % Cs is incorporated in NiO_x, which is consistent with the estimation from EDXS (0.7 at. %).

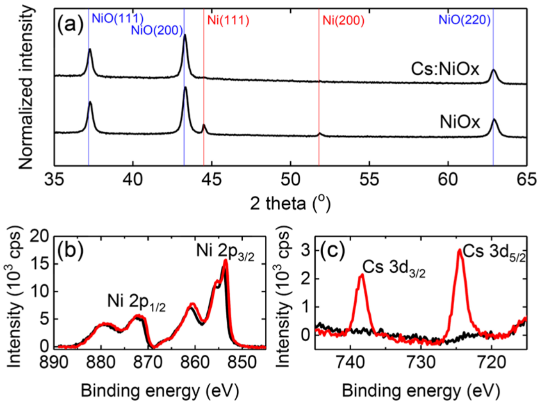

Figure 1. (a) Normalized XRD patters of NiO_x and Cs-incorporated NiO_x (Cs/NiO_x). (b) Ni 2p and (c) Cs 3d XPS spectra of NiO_x and Cs/NiO_x. The sample was prepared as a powder in the same manner as for the film. Black and red lines indicate NiO_x and Cs/NiO_x, respectively.

A 25 nm thick dense NiO_x film was prepared by a solution process and employed in the device. The morphologies of the NiO_x and Cs-incorporated NiO_x films on the fluorine-doped tin oxide (FTO) glass are shown in Figure S2. It is found that the Cs-incorporated NiO_x layer (Figure S2b) results in more rough surface morphology compared to the NiO_x layer (Figure S2a). However, it makes little difference in the perovskite morphology whether the perovskite is grown on NiO_x (Figure S2c) or on Cs-incorporated NiO_x (Figure S2d). Both perovskite films deposited by the antisolvent method[9] produce flat and large grain whose size ranges from 50 to 400 nm.

Perovskite films deposited on the NiO_x and Cs-incorporated NiO_x substrates showed similar absorbance spectra, which are shown in Figure 2a, indicating a negligible difference in light harvesting efficiency. Photoluminescence (PL) was measured for perovskite films to investigate the effect of the NiO_x layer on charge separation. For perovskites, 450 nm was used as an excitation wavelength, and the incidence was made from the FTO/NiO_x (glass) side for steady-state PL. PL spectra of the perovskite film deposited on the glass substrate without any quenching layer are shown in Figure S2a. The radiative recombination is mainly determined by the band gap energy,

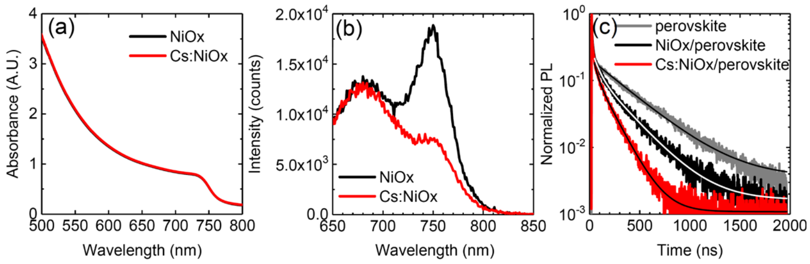

Figure 2. (a) Absorbance and (b) PL spectra of the perovskite film deposited on NiO_x (black) and Cs-incorporated NiO_x (red) substrates. (c) TR-PL of the perovskite film based on the glass (gray), FTO/NiO_x (black), and FTO/Cs-incorporated NiO_x (red) substrates with fitted curves.

DOI: 10.1021/acsomega.7b01179
ACS Omega 2017, 2, 9074−9079

leading to a large emission at 750 nm which corresponds to the band gap of the perovskite. The PL peak at 680 nm comes from the FTO glass itself (Figure S3b). In Figure 2b, the perovskite attached to the NiO_x layer shows a significantly decreased PL at 750 nm, which is attributed to the carrier injection to the adjacent selective contact inhibiting the radiative recombination in the material. NiO_x is used as a hole selective contact and is responsible for hole separation. Noticeably, perovskites with the NiO_x layer still showed a clear peak at 750 nm because of the remaining hole carriers in the perovskites. It is found that Cs-incorporated NiO_x enables holes to be separated more efficiently, diminishing the PL intensity at 750 nm even more than bare NiO_x (Figure 2b).

Time-resolved PL (TR-PL) measurements were carried out to have more insight on the Cs-doping effect. TR-PL spectra of perovskite films with different substrates are shown in Figure 2c. A 408 nm single wavelength was used as an excitation source, and 750 nm of wavelength was monitored as a result of recombination. The TR-PL spectra were fitted to estimate the PL life time quantitatively by using one- or two-component exponential decay.[31,32] The fitting results and the estimated values from fittings are shown in Figure 2c and Table 1. For the perovskite film without NiO_x, a one-component exponential decay fit well to the results, indicating that a first order is dominant in the perovskite layer itself. However, the one-exponential decay brought a considerable discrepancy in the case of the perovskite film with the NiO_x (Cs/NiO_x) substrate, where a two-component exponential decay was used to fit the results. While the slow decay component (τ_1) is still found in a comparable range with the one observed from the bare perovskite film, the fast decay component (τ_2) is newly developed by attaching the quenching layer. Consequently, the slow decay component (τ_1) is mostly determined by the recombination of carriers in the perovskite,[31,32] and the fast decay component (τ_2) is affected by quenching of the carriers[32] because of the hole selective contact (NiO_x) in this study. As expected, the perovskite film on the glass without any quenching layer has the longest τ_1 of 349.1 ns. Adding the NiO_x layer to the perovskite film generates the fast decay component (τ_2) of 58.0 ns because of the effective hole quenching at the interface, which seems to have an effect on free carrier recombination in bulk perovskites with a shortening of τ_1 to 263.4 nm. The shortened τ_1 could be attributed to the increased electron density in the vicinity of the hole selective contact, which can sufficiently facilitate the recombination near the contact. Both decay components are even more reduced to 146.5 ns for τ_1 and to 32.5 ns for τ_2 by employing Cs into NiO_x, indicating that the hole transfer at the interface becomes more accelerated for Cs/NiO_x. The observed improved hole separation could be ascribed to either the increased interface area (Figure S2b) or the removal of the Ni phase by Cs incorporation.

Table 1. Carrier Life Time of Perovskite Films According to the TR-PL Fitting with Exponential Decay

time component	perovskite (ns)	NiO_x/perovskite (ns)	Cs/NiO_x/perovskite (ns)
τ_1	349.1	262.4	146.5
τ_2		58.0	32.5

We found that employing Cs into NiO_x leads to more efficient hole injection at the interface according to PL data. In terms of charge collection, the charge transfer in the selective contact medium itself should be considered at the same time. The resistivity is increased from 8.1 × 10^4 Ω cm for NiO_x to 15.2 × 10^4 Ω cm for Cs/NiO_x. The increase in resistivity can be attributed to the synthesis method,[33,34] the formation of secondary phases,[35] or to scattering effects[35] as reported earlier for Li-doped NiO_x. Although there are no electrical properties available for $Cs_{0.1}NiO_2$ or Cs_2NiO_2, taking into account that Cs_2O is a n-type semiconductor and Cs_2O_2 is an insulator,[36,37] the inclusion of Cs into NiO_x could reduce the p-type conductivity and thus increase the resistivity. However, the slight increase in resistivity by Cs incorporation seems unlikely to exceed other beneficial effects by Cs incorporation.

The photovoltaic performance was measured based on the inverted structure, where NiO_x or Cs/NiO_x was employed as the hole transport material, and PCBM was used as the electron transport material (inset of Figure 3a). Figure 3a shows the I–V curves for the perovskite solar cells with NiO_x and Cs/NiO_x, and the corresponding photovoltaic parameters are shown in Table 2. The statistical photovoltaic parameters are shown in Figure S4 and Table S2. The I–V curves were obtained with a forward scan from open circuit to short circuit. Both devices show a hysteresis-free behavior even with 1 ms for the voltage settling time, as shown in Figure S5, indicating that the steady-state condition is rapidly reached. The device with Cs/NiO_x demonstrates a higher PCE of 17.2% (15.9% for average) than that of 15.3% (13.8% for average) for the NiO_x, mainly because of the higher short-circuit photocurrent density (J_{sc}) and the fill factor (FF). The Cs/NiO_x device shows 21.4 mA/cm^2 of J_{sc} and 0.78 of FF, whereas 20.4 mA/cm^2 of J_{sc} and 0.72 of FF are obtained from the NiO_x device. Considering the fact that the light absorbance is comparable for both films (Figure 2a), the efficient and fast charge injection from the perovskite to the hole selective contact is dominantly responsible for the higher J_{sc} for Cs/NiO_x according to PL results (Figure 2b,c).

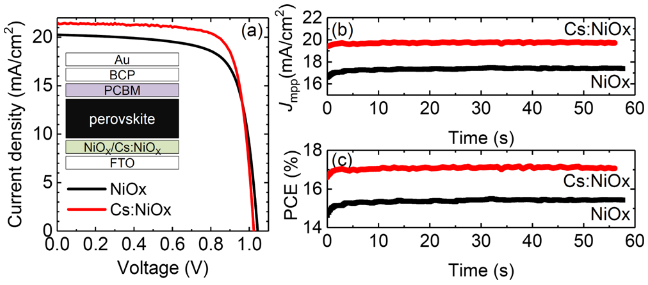

Figure 3. (a) I–V curves of perovskite solar cells based on NiO_x (black) and Cs-incorporated NiO_x (red). The inset figure in (a) shows the schematic structure of the inverted device. Time-dependent (b) photocurrent density and (c) PCE at the maximum power point.

Table 2. Photovoltaic Parameters of Perovskite Solar Cells Based on NiO_x and Cs-Incorporated NiO_x

	J_{sc} (mA/cm^2)	V_{oc} (V)	FF	PCE (%)
NiO_x	20.4	1.04	0.72	15.3
Cs/NiO_x	21.4	1.03	0.78	17.2

In Figure 3b,c, the dependence of photocurrent density at the maximum power point (J_{mpp}) and the corresponding evolution of PCE with time are shown. J_{mpp} is a good indicator for the FF. The Cs/NiO_x device with a higher FF obviously demonstrated higher J_{mpp}. It is noted that both inverted devices show a stable behavior once they reach the saturation point. It is clearly contrary to the behavior of the normal structure whose PCE often gradually goes down after reaching the highest PCE. It must be related to the charge-transfer mechanism at the interface with the selective contact. The understanding of the detailed mechanism is beyond the scope of the current study and will be handled separately. The saturated J_{mpp} reaches 19.7 mA/cm^2 for Cs/NiO$_x$ and 17.4 mA/cm^2 for NiO$_x$ (Figure 3b), consequently leading to a PCE of 17.1 and 15.4% for Cs/NiO$_x$ and NiO$_x$ (Figure 3c), respectively.

Impedance spectroscopy (IS) measurements were performed to investigate the recombination resistance, accounting for FF and J_{mpp}. The IS measurement was carried out under the illumination of a white light-emitting diode (LED) with a forward bias ranging from short-circuit to near-open-circuit voltage. Recently, various equivalent circuits have been reported to assign each element to unique characteristics of perovskite solar cells such as ionic movement and polarization.[38−40] However, these are still controversial. In this study, we used the most common simplified circuit, which is composed of R and R−C circuits in series. Figure 4 shows the recombination resistance (R_{rec}) obtained by fitting the Nyquist plot observed from the low frequency range (Figure S6).[41,42] The device with Cs/NiO$_x$ shows higher R_{rec} at 0.0−0.8 V compared to the one with NiO$_x$. The difference in R_{rec} is mostly governed by the recombination near the hole selective contact because the only difference between the two devices is the NiO$_x$ contact. Therefore, the charge recombination is significantly suppressed by the Cs/NiO$_x$ layer with a negligible Ni phase, which could sufficiently act as a recombination center. Otherwise, the accumulated carriers due to the low hole extraction by NiO$_x$, compared to Cs/NiO$_x$, can be responsible for the accelerated recombination in bulk perovskites,[42] leading to the low R_{rec} for NiO$_x$. The difference between R_{rec} values gradually increases toward the higher voltage region which determines the FF and J_{mpp}. However, the R_{rec} tendency is reversed near V_{oc}, which seems to be responsible for the slightly lower V_{oc} for the device with Cs/NiO$_x$, implying that the Cs incorporation induces a positive shift in the valence band. The R_{rec} results are well in accordance with the photovoltaic parameters.

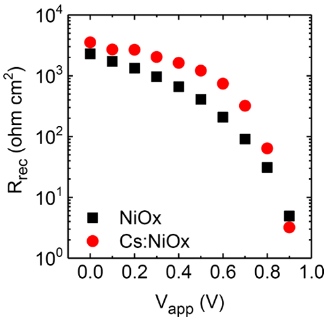

Figure 4. Recombination resistance of perovskite solar cells based on NiO$_x$ (black squares) and Cs-incorporated NiO$_x$ (red circles) under illumination.

In conclusion, the effect of Cs-incorporated NiO$_x$ on the performance of the inverted perovskite solar cells was studied. An employment of Cs in the NiO$_x$ layer was found to effectively suppress the development of an Ni phase in the NiO$_x$ layer. Furthermore, the Cs-incorporated NiO$_x$ layer enabled holes in perovskites to be efficiently separated and collected, which significantly impeded the recombination at the interface by lowering the hole concentration. Consequently, the perovskite solar cells based on Cs-incorporated NiO$_x$ demonstrated higher PCE mainly because of the higher photocurrent density and FF.

EXPERIMENTAL SECTION

Preparation of Perovskite Precursor Solution. 1.5 M lead iodide (TCI) was prepared where the solvent was a mixture of dimethylformamide (DMF, Acros) and dimethyl sulfoxide (DMSO, Acros) (DMF/DMSO = 4:1 volume ratio). Formamidinium iodide (Dyesol) was added to the 1.5 M PbI$_2$ solution with a 9% excess molar ratio for PbI$_2$. A mixture of 1.5 M lead bromide (TCI) and methylammonium bromide (Dyesol) was prepared in the same manner as for 9 mol % excess Pb and mixed solvent. 1.5 M cesium iodide (ABCR, 99.998%) was prepared with DMSO. To make a perovskite precursor solution based on mixed triple cations and double halides, the prepared FAPbI$_3$, MAPbBr$_3$, and CsI solutions were mixed in a ratio of 5:1:0.3.

Preparation of Device. An FTO substrate (Nippon, 10 Ω/sq) was sequentially sonicated for 15 min in a detergent (2% diluted in DIW, Hellmanex III, Hellma GmbH), DIW, and ethanol. The cleaned FTO glass was exposed to UV/ozone treatment for 10 min. 0.1 M nickel nitrate hexahydrate (Sigma, 99.999%) in 2-methoxy ethanol (Roth, 99%) was deposited on the FTO glass using spin-coating at 4000 rpm for 20 s, which was followed by heating at 500 °C for 1 h with an increasing temperature rate of 16 °C/min. A closed box furnace without any gas flow was used for the annealing process. In the case of the cesium-mixed nickel precursor solution, cesium nitrate (Acros, 99.99%) was added to the nickel solution according to the required atomic ratio. The prepared perovskite solution was deposited on the NiO$_x$ substrate using an antisolvent method.[9] Briefly, 100 μL of chlorobenzene (Aldrich) was dropped on the substrate at the end of spinning (10 s before termination) of the perovskite precursor solution. The substrate coated with the perovskite precursor solution was heated at 100 °C for 50 min to be converted into the perovskite black phase. A PCBM (1-material) solution (20 mg/1 mL chlorobenzene) was deposited on the cooled down perovskite substrate by spin-coating at 5000 rpm for 30 s. Post-heat treatment for PCBM was carried out at 100 °C for 10 min. A bathocuproine (BCP, TCI, 98.0%) solution (0.5 mg/1 mL ethanol) was deposited for the hole blocking layer on the top of annealed PCBM using a spin-coater with 6000 rpm for 20 s. Gold was evaporated to make a ca. 75 nm-thick top electrode at 10^{-6} Torr. All the spin-coating procedures including perovskites, PCBM, and BCP were carried out in the glovebox filled with dry air.

Measurement. Current−voltage (I−V) curves and maximum power tracking were measured by a solar simulator (Oriel, OPS-A500) equipped with a 450 W xenon light source. A Schott K113 Tempax filter (PräzisionsGlas & Optik GmbH) was used to reduce the mismatch between the Xe lamp and a standard AM 1.5G light spectrum. A calibration for the light intensity was carried out prior to each measurement by the aid of a silicon reference cell equipped with an *IR*-cutoff filter (KG3, Schott). IS measurements were performed by a potentiostat (BioLogic, MPG 2) under a white LED light source. dc bias voltage was given from 0 to 0.8 V with a potential step of 100 mV. Sinusoidal ac voltage (20 mV)

DOI: 10.1021/acsomega.7b01179
ACS Omega 2017, 2, 9074−9079

ranging from 1 MHz to 1 Hz was put on the dc voltage. The measured data were fitted using ZView software with a simplified equivalent circuit composed of resistance (*R*) and three *R*−*C* (resistance and capacitance in parallel) components in series. The recombination resistance was obtained from the last *R*−*C* component corresponding to the low frequency. To avoid scattering effects of the glass substrate, an aperture with the black metal was attached to the device during all measurements (*I*−*V*, maximum power point tracking and IS) under illumination. The active area for the devices was 0.16 cm^2. Absorption spectroscopy measurements were performed with a UV−vis−NIR spectrophotometer (Cary5, Varian). PL was measured by Fluorolog 322 (Horiba JobinYbon Ltd.). For the steady-state PL measurement, a wavelength of 450 nm was used for the excitation. For TR-PL, a single wavelength of 408 nm (N-405 L, Horiba) with 1 MHz was used for the excitation, and the resulting TR-PL was monitored at 750 nm. High-resolution scanning electron microscopy (HR-SEM) and EDXS were measured by ZEISS Merlin. XRD of the sample was measured using an Empyrean (PANalytical) instrument equipped with a ceramic tube (Cu anode, λ = 1.54060 Å) and PIXel^{1D} (PANalytical). XRD data were analyzed using HighScore Plus software. HR-SEM images were obtained by ZEISS Merlin. XPS measurements were carried out using a PHI VersaProbe II scanning XPS microprobe (Physical Instruments AG, Germany). The samples for XRD and XPS measurements were prepared as powders by using the same precursor solutions for the NiO_x films. The precursor solution was coated on the large glass substrate and annealed in the same manner as for the NiO_x film. After the annealing process, the products were removed from the glass substrate and collected as powders. The conductivity study was made by a Precision LCR Meter (Agilent E4980A) at room temperature in ambient air.

■ ASSOCIATED CONTENT

Supporting Information

The Supporting Information is available free of charge on the ACS Publications website at DOI: 10.1021/acsomega.7b01179.

> Crystallographic parameters of NiO and $Cs_{0.1}NiO_2$, Ni $2p_{3/2}$ XPS spectra of milled NiO_x, surface SEM images, PL spectra, statistical photovoltaic parameters, *I*−*V* hysteresis curve, and Nyquist plots (PDF)

■ AUTHOR INFORMATION

Corresponding Authors

*E-mail: hui-seon.kim@epfl.ch (H.-S.K.).
*E-mail: hagfeldt@epfl.ch (A.H.).

ORCID

Hui-Seon Kim: 0000-0002-9928-3033
Monica Lira-Cantu: 0000-0002-3393-7436
Michael Grätzel: 0000-0002-0068-0195

Notes

The authors declare no competing financial interest.

■ ACKNOWLEDGMENTS

We thank the financial support from the SNSF NRP70 "Energy Turnaround," and the GRAPHENE project supported by the European Commission Seventh Framework Programme under contract 604391 is gratefully acknowledged. H.-S.K. is grateful for the postdoctoral fellowship grant (NRF-2016R1A6A3A03012393), to the Spanish MINECO through the Severo Ochoa Centers of Excellence Program under Grant SEV-2013-0295 for the Postdoctoral contract to H.X., for the grant ENE2016-79282-C5-2-R and the OrgEnergyExcelence Network CTQ2016-81911-REDT, to the Agència de Gestiód'AjutsUniversitarisi de Recerca for the support to the consolidated Catalonia research group 2014SGR-1212 and the Xarxa de Referènciaen Materials Avançats per a l'Energia (Xarmae), and to the COST Action StableNextSol project MP1307.

■ REFERENCES

(1) Kim, H.-S.; Lee, C.-R.; Im, J.-H.; Lee, K.-B.; Moehl, T.; Marchioro, A.; Moon, S.-J.; Humphry-Baker, R.; Yum, J.-H.; Moser, J. E.; et al. Lead Iodide Perovskite Sensitized All-Solid-State Submicron Thin Film Mesoscopic Solar Cell with Efficiency Exceeding 9%. *Sci. Rep.* **2012**, *2*, 591.

(2) Lee, M. M.; Teuscher, J.; Miyasaka, T.; Murakami, T. N.; Snaith, H. J. Efficient Hybrid Solar Cells Based on Meso-Superstructured Organometal Halide Perovskites. *Science* **2012**, *338*, 643−647.

(3) Burschka, J.; Pellet, N.; Moon, S.-J.; Humphry-Baker, R.; Gao, P.; Nazeeruddin, M. K.; Grätzel, M. Sequential Deposition as a Route to High-Performance Perovskite-Sensitized Solar Cells. *Nature* **2013**, *499*, 316−319.

(4) Jeon, N. J.; Noh, J. H.; Kim, Y. C.; Yang, W. S.; Ryu, S.; Seok, S. I. Solvent Engineering for High-Performance Inorganic−Organic Hybrid Perovskite Solar Cells. *Nat. Mater.* **2014**, *13*, 897−903.

(5) Liu, M.; Johnston, M. B.; Snaith, H. J. Efficient Planar Heterojunction Perovskite Solar Cells by Vapour Deposition. *Nature* **2013**, *501*, 395−398.

(6) Nie, W.; Tsai, H.; Asadpour, R.; Blancon, J.-C.; Neukirch, A. J.; Gupta, G.; Crochet, J. J.; Chhowalla, M.; Tretiak, S.; Alam, M. A.; et al. High-Efficiency Solution-Processed Perovskite Solar Cells with Millimeter-Scale Grains. *Science* **2015**, *347*, 522−525.

(7) Li, X.; Bi, D.; Yi, C.; Decoppet, J.-D.; Luo, J.; Zakeeruddin, S. M.; Hagfeldt, A.; Gratzel, M. A Vacuum Flash-Assisted Solution Process for High-Efficiency Large-Area Perovskite Solar Cells. *Science* **2016**, *353*, 58−62.

(8) Ahn, N.; Son, D.-Y.; Jang, I.-H.; Kang, S. M.; Choi, M.; Park, N.-G. Highly Reproducible Perovskite Solar Cells with Average Efficiency of 18.3% and Best Efficiency of 19.7% Fabricated via Lewis Base Adduct of Lead(II) Iodide. *J. Am. Chem. Soc.* **2015**, *137*, 8696−8699.

(9) Saliba, M.; Matsui, T.; Domanski, K.; Seo, J.-Y.; Ummadisingu, A.; Zakeeruddin, S. M.; Correa-Baena, J.-P.; Tress, W. R.; Abate, A.; Hagfeldt, A.; et al. Incorporation of Rubidium Cations into Perovskite Solar Cells Improves Photovoltaic Performance. *Science* **2016**, *354*, 206−209.

(10) https://www.nrel.gov/pv/assets/images/efficiency-chart.png.

(11) Unger, E. L.; Hoke, E. T.; Bailie, C. D.; Nguyen, W. H.; Bowring, A. R.; Heumüller, T.; Christoforo, M. G.; McGehee, M. D. Hysteresis and Transient Behavior in Current−Voltage Measurements of Hybrid-Perovskite Absorber Solar Cells. *Energy Environ. Sci.* **2014**, *7*, 3690−3698.

(12) Kim, H.-S.; Park, N.-G. Parameters Affecting I−V Hysteresis of $CH_3NH_3PbI_3$ Perovskite Solar Cells: Effects of Perovskite Crystal Size and Mesoporous TiO_2 Layer. *J. Phys. Chem. Lett.* **2014**, *5*, 2927−2934.

(13) Chen, B.; Yang, M.; Zheng, X.; Wu, C.; Li, W.; Yan, Y.; Bisquert, J.; Garcia-Belmonte, G.; Zhu, K.; Priya, S. Impact of Capacitive Effect and Ion Migration on the Hysteretic Behavior of Perovskite Solar Cells. *J. Phys. Chem. Lett.* **2015**, *6*, 4693−4700.

(14) Kim, H.-S.; Jang, I.-H.; Ahn, N.; Choi, M.; Guerrero, A.; Bisquert, J.; Park, N.-G. Control of I−V Hysteresis in $CH_3NH_3PbI_3$ Perovskite Solar Cell. *J. Phys. Chem. Lett.* **2015**, *6*, 4633−4639.

(15) Xiao, Z.; Yuan, Y.; Shao, Y.; Wang, Q.; Dong, Q.; Bi, C.; Sharma, P.; Gruverman, A.; Huang, J. Giant Switchable Photovoltaic Effect in Organometal Trihalide Perovskite Devices. *Nat. Mater.* **2015**, *14*, 193−198.

(16) Yuan, Y.; Huang, J. Ion Migration in Organometal Trihalide Perovskite and Its Impact on Photovoltaic Efficiency and Stability. *Acc. Chem. Res.* **2016**, *49*, 286−293.

(17) Guerrero, A.; You, J.; Aranda, C.; Kang, Y. S.; Garcia-Belmonte, G.; Zhou, H.; Bisquert, J.; Yang, Y. Interfacial Degradation of Planar Lead Halide Perovskite Solar Cells. *ACS Nano* **2016**, *10*, 218−224.

(18) Zhao, X.; Kim, H.-S.; Seo, J.-Y.; Park, N.-G. Effect of Selective Contacts on the Thermal Stability of Perovskite Solar Cells. *ACS Appl. Mater. Interfaces* **2017**, *9*, 7148−7153.

(19) Malinauskas, T.; Tomkute-Luksiene, D.; Sens, R.; Daskeviciene, M.; Send, R.; Wonneberger, H.; Jankauskas, V.; Bruder, I.; Getautis, V. Enhancing Thermal Stability and Lifetime of Solid-State Dye-Sensitized Solar Cells via Molecular Engineering of the Hole-Transporting Material Spiro-OMeTAD. *ACS Appl. Mater. Interfaces* **2015**, *7*, 11107−11116.

(20) Chen, W.; Wu, Y.; Yue, Y.; Liu, J.; Zhang, W.; Yang, X.; Chen, H.; Bi, E.; Ashraful, I.; Grätzel, M.; et al. Efficient and Stable Large-Area Perovskite Solar Cells with Inorganic Charge Extraction Layers. *Science* **2015**, *350*, 944−948.

(21) Jung, J. W.; Chueh, C.-C.; Jen, A. K.-Y. A Low-Temperature, Solution-Processable, Cu-Doped Nickel Oxide Hole-Transporting Layer via the Combustion Method for High-Performance Thin-Film Perovskite Solar Cells. *Adv. Mater.* **2015**, *27*, 7874−7880.

(22) Xue, Q.; Bai, Y.; Liu, M.; Xia, R.; Hu, Z.; Chen, Z.; Jiang, X.-F.; Huang, F.; Yang, S.; Matsuo, Y.; et al. Dual Interfacial Modifications Enable High Performance Semitransparent Perovskite Solar Cells with Large Open Circuit Voltage and Fill Factor. *Adv. Energy Mater.* **2017**, *7*, 1602333.

(23) Jeng, J.-Y.; Chen, K.-C.; Chiang, T.-Y.; Lin, P.-Y.; Tsai, T.-D.; Chang, Y.-C.; Guo, T.-F.; Chen, P.; Wen, T.-C.; Hsu, Y.-J. Nickel Oxide Electrode Interlayer in $CH_3NH_3PbI_3$ Perovskite/PCBM Planar-Heterojunction Hybrid Solar Cells. *Adv. Mater.* **2014**, *26*, 4107−4113.

(24) Hu, L.; Peng, J.; Wang, W.; Xia, Z.; Yuan, J.; Lu, J.; Huang, X.; Ma, W.; Song, H.; Chen, W.; Cheng, Y.-B.; Tang, J. Sequential Deposition of $CH_3NH_3PbI_3$ on Planar NiO Film for Efficient Planar Perovskite Solar Cells. *ACS Photonics* **2014**, *1*, 547−553.

(25) Wang, K.-C.; Jeng, J.-Y.; Shen, P.-S.; Chang, Y.-C.; Diau, E. W.-G.; Tsai, C.-H.; Chao, T.-Y.; Hsu, H.-C.; Lin, P.-Y.; Chen, P.; Guo, T.-F.; Wen, T.-C. p-type Mesoscopic Nickel Oxide/Organometallic Perovskite Heterojunction Solar Cells. *Sci. Rep.* **2014**, *4*, 4756.

(26) Chen, D.-H.; Hsieh, C.-H. Synthesis of Nickel Nanoparticles in Aqueous Cationic Surfactant Solutions. *J. Mater. Chem.* **2002**, *12*, 2412−2415.

(27) Guo, W.; Hui, K. N.; Hui, K. S. High Conductivity Nickel Oxide Thin Films by a Facile Sol−Gel Method. *Mater. Lett.* **2013**, *92*, 291−295.

(28) Ubic, R. Revised Method for the Prediction of Lattice Constants in Cubic and Pseudocubic Perovskites. *J. Am. Ceram. Soc.* **2007**, *90*, 3326−3330.

(29) Rajagopal Reddy, V.; Sekhar Reddy, P. R.; Neelakanta Reddy, I.; Choi, C.-J. Microstructural, Electrical and Carrier Transport Properties of Au/NiO/n-GaN Heterojunction with a Nickel Oxide Interlayer. *RSC Adv.* **2016**, *6*, 105761−105770.

(30) Zhu, Y.; Mcbride, J. D.; Hansen, T. A.; Beebe, T. P. Controlled Production of Molecule Corrals Using Cesium Ion Bombardment: A TOF−SIMS, XPS, and STM Study. *J. Phys. Chem. B* **2001**, *105*, 2010−2018.

(31) Chen, Q.; Zhou, H.; Song, T.-B.; Luo, S.; Hong, Z.; Duan, H.-S.; Dou, L.; Liu, Y.; Yang, Y. Controllable Self-Induced Passivation of Hybrid Lead Iodide Perovskites Toward High Performance Solar Cells. *Nano Lett.* **2014**, *14*, 4158−4163.

(32) Li, Y.; Meng, L.; Yang, Y.; Xu, G.; Hong, Z.; Chen, Q.; You, J.; Li, G.; Yang, Y.; Li, Y. High-Efficiency Robust Perovskite Solar Cells on Ultrathin Flexible Substrates. *Nat. Commun.* **2016**, *7*, 10214.

(33) Dutta, T.; Gupta, P.; Gupta, A.; Narayan, J. Effect of Li Doping in NiO Thin Films on Its Transparent and Conducting Properties and Its Application in Heteroepitaxial p-n Junctions. *J. Appl. Phys.* **2010**, *108*, 083715.

(34) Jang, W.-L.; Lu, Y.-M.; Hwang, W.-S.; Chen, W.-C. Electrical Properties of Li-Doped NiO Films. *J. Eur. Ceram. Soc.* **2010**, *30*, 503−508.

(35) Joseph, D. P.; Saravanan, M.; Muthuraaman, B.; Renugambal, P.; Sambasivam, S.; Raja, S. P.; Maruthamuthu, P.; Venkateswaran, C. Spray Deposition and Characterization of Nanostructured Li Doped NiO Thin Films for Application in Dye-Sensitized Solar Cells. *Nanotechnology* **2008**, *19*, 485707.

(36) Haberland, H. *Clusters of Atoms and Molecules: Theory, Experiment, and Clusters of Atoms*; Springer Science & Business Media, 2013; p 422.

(37) Hass, G.; Francombe, M. H.; Vossen, J. L. *Physics of Thin Films: Advances in Research and Development*; Academic Press, 2017; p 340.

(38) Bai, Y.; Dong, Q.; Shao, Y.; Deng, Y.; Wang, Q.; Shen, L.; Wang, D.; Wei, W.; Huang, J. Enhancing Stability and Efficiency of Perovskite Solar Cells with Crosslinkable Silane-Functionalized and Doped Fullerene. *Nat. Commun.* **2016**, *7*, 12806.

(39) Ghahremanirad, E.; Bou, A.; Olyaee, S.; Bisquert, J. Inductive Loop in the Impedance Response of Perovskite Solar Cells Explained by Surface Polarization Model. *J. Phys. Chem. Lett.* **2017**, *8*, 1402−1406.

(40) Guerrero, A.; Garcia-Belmonte, G.; Mora-Sero, I.; Bisquert, J.; Kang, Y. S.; Jacobsson, T. J.; Correa-Baena, J.-P.; Hagfeldt, A. Properties of Contact and Bulk Impedances in Hybrid Lead Halide Perovskite Solar Cells Including Inductive Loop Elements. *J. Phys. Chem. C* **2016**, *120*, 8023−8032.

(41) Kim, H.-S.; Seo, J.-Y.; Park, N.-G. Impact of Selective Contacts on Long-Term Stability of $CH_3NH_3PbI_3$ Perovskite Solar Cells. *J. Phys. Chem. C* **2016**, *120*, 27840−27848.

(42) Juarez-Perez, E. J.; Wuβler, M.; Fabregat-Santiago, F.; Lakus-Wollny, K.; Mankel, E.; Mayer, T.; Jaegermann, W.; Mora-Sero, I. Role of the Selective Contacts in the Performance of Lead Halide Perovskite Solar Cells. *J. Phys. Chem. Lett.* **2014**, *5*, 680−685.

DOI: 10.1021/acsomega.7b01179
ACS Omega 2017, 2, 9074−9079